IEEE Access
Multidisciplinary | Rapid Review | Open Access Journal

Received 3 February 2023, accepted 24 February 2023, date of publication 3 March 2023, date of current version 13 March 2023.

Digital Object Identifier 10.1109/ACCESS.2023.3251987

RESEARCH ARTICLE

Communication-Less Receiver-Side Resonant Frequency Tuning for Magnetically Coupled Wireless Power Transfer Systems

KENTARO MATSUURA, (Graduate Student Member, IEEE), DAISUKE KOBUCHI, (Graduate Student Member, IEEE), YOSHIAKI NARUSUE, (Member, IEEE), AND HIROYUKI MORIKAWA, (Member, IEEE)

Graduate School of Engineering, The University of Tokyo, Tokyo 113-8656, Japan

Corresponding author: Yoshiaki Narusue (narusue@mlab.t.u-tokyo.ac.jp)

This work was supported in part by JSPS (Japan Society for the Promotion of Science) KAKENHI Grant Numbers JP20H02143 and JP21K14154.

ABSTRACT Compensating for deviations in the resonant frequency is crucial in magnetic resonance coupling wireless power transfer (WPT) systems. Thus, this study proposes a communication-less receiver-side resonant frequency-tuning scheme that compensates for the reactance in the receiver without communicating with the transmitter. The proposed scheme comprises an inductor-capacitor-capacitor compensation topology at the transmitter and a half-bridge circuit at the receiver, whose operating phase is set to be orthogonal to the receiver current. Resonant frequency tuning can be achieved by adjusting the DC voltage applied to the half-bridge circuit to maximize the power received at the load. The reactance compensation ability of the proposed scheme is analyzed through experiments on a 200 kHz WPT system. When the secondary capacitance deviated from −20% to +20%, the efficiency degradation was maintained within 6.7% with the proposed scheme, whereas the efficiency degraded by up to 33.3% without compensation.

INDEX TERMS Magnetic resonance, reactance compensation, resonant frequency, variable reactor, wireless power transfer.

I. INTRODUCTION

Wireless power transfer (WPT) systems are adopted as safe and convenient modes of power supply in practical applications. Among the various WPT technologies, WPT via magnetic resonance coupling (MRC) is currently considered the most suitable mechanism for high-efficiency mid-range transmissions [1], [2], [3], [4]. WPT via MRC (MRC-WPT) can be applied in various fields ranging from low-power charging for mobile devices to high-power charging for electric vehicles [5], [6], [7], [8].

Foreign objects, such as dielectric materials, metallic objects, or ferromagnetic materials, near the transmitter and receiver coils, cause inductance changes, leading to resonant frequency deviation and a consequent reduction in the power and efficiency [9]. In MRC-WPT systems, resonant frequency deviation is a significant concern for practical application. The capacitors and inductors used in compensation circuits exhibit natural tolerance owing to manufacturing errors and aging, resulting in power reduction and power transfer efficiency degradation [10].

Numerous impedance tuning methods to adjust the resonant frequency have been proposed; for example, a variable capacitor adjusted by a stepping motor [11] or a reactor matrix with several capacitors, inductors, and mechanical relay switches [12], [13], [14]. However, mechanical parts consume considerable power, are bulky, and slow in response. In [15], PIN diodes were used as switches instead of mechanical relays to achieve high-speed operation; however, their current rating was significantly low.

To overcome these limitations, pulse-width modulation controlled switched capacitors [16], [17], [18], [19] and field-effect transistor (FET) bridge-based variable reactors [20], [21], [22], [23], [24], [25] can be used as they do

The associate editor coordinating the review of this manuscript and approving it for publication was Kai Song.

not require mechanical components, can handle high power, and can be miniaturized. Among them, the FET bridge-based variable reactor is characterized by its ease of control at the transmitter side; current and voltage phases must not be measured for control. Its reactance automatically converges to the optimal value for resonance correction only by shifting the switching phase by constant degrees from the transmitter inverter.

Conventional studies on FET bridge-based variable reactors mainly focused on the transmitter side [20]. However, this study focuses on the operation of FET bridge-based variable reactors at the receiver side. The effectiveness of using a FET bridge-based variable reactor apart from a transmitter has been demonstrated. In [21] and [22], a FET bridge-based variable reactor was applied with a repeater resonator to retune the resonant frequency. In [23], a receiver-side FET bridge-based variable reactor was used to compensate for the detuning of the resonant frequency owing to natural tolerance and cross-coupling among multiple receivers. In [25], the 6.78-MHz operation of a FET bridge-based variable reactor in a receiver was demonstrated.

The operation of the FET bridge-based variable reactor apart from the transmitter has an unresolved issue (distribution of the clock). Clock synchronization between the transmitter and receiver requires nanosecond-order precision for kHz-band systems. The requirement for precision is expected to be more stringent for MHz-band systems, rendering its implementation with wireless communication systems challenging. Wired clock distribution was adopted in [21]; however, wireless systems do not use wires. Reference [22] utilized infrared (IR) communication, which involved the transmission of the gate-drive signal of the transmitter to the receiver. However, the optical components to transmit and receive light must be exposed, rendering the device-case design complex. An auxiliary measurement coil with a decoupling transformer [26], [27] can be used to measure the voltage induced by the transmitter; however, auxiliary coils are susceptible to cross-coupling with the receiver coil, which limits the coil geometry design.

An alternative approach to avoid the wireless link for clock distribution is to generate the clock signal at the receiver using the receiver current. In [28] and [29], the reactance was compensated for using an active rectifier on the secondary side. The gate-drive signal for the active rectifier was generated from the receiver current. However, the control of this method must measure the output voltage and current as well as the phase angle of the receiver current and the induced voltage, which requires an expensive AC current sensor and complex calculations. In particular, the measurement of the induced voltage is impractical because it requires an accurate value of the inductance of the receiver coil, which will be deviated during operation.

This study proposes a communication-less receiver-side resonant frequency tuning scheme with a FET bridge-based variable reactor. First, we changed the reference of the gate-drive signal for the FET bridge-based variable reactor from the transmitter to the receiver; the phase of the gate-drive signal for the half-bridge circuit on the receiver side is set to be orthogonal to the phase of the receiver current. Thus, we eliminated the clock distribution from the transmitter via a wireless communication link. Second, we designed the reactance control scheme such that it can be performed without using any information from the transmitter; an inductor-capacitor-capacitor (LCC) compensation topology was installed at the transmitter to operate the receiver circuit with constant voltage (CV) characteristics. Thus, we can use the received power as the objective function to detect the optimum DC voltage to compensate for the reactance in the receiver.

The strengths of the proposed scheme are summarized as follows: (1) Throughout the control process, any information from the transmitter, including the clock, is not required. (2) The only control parameter required is the DC received power at the load, which can be easily measured.

The fundamental concept of this scheme was described in [30]. In this study, we perform extended theoretical analyses and experimental validations. Particularly,

1) we detailedly describe the circuit equations of the proposed scheme.
2) we demonstrate the hardware implementation, including the circuit configuration to generate the gate-drive signal for the variable reactor and the automatic DC-voltage-adjustment strategy.
3) we conduct comprehensive evaluations for various reactance deviations and loss distribution analysis of the proposed scheme.

The remainder of this paper is organized as follows. Section II describes the working principle of the proposed scheme and presents the theoretical analysis using circuit equations. Section III reports the measurement and simulation results to validate the effectiveness of the proposed scheme. Section IV concludes the paper.

II. COMMUNICATION-LESS RECEIVER-SIDE RESONANT FREQUENCY TUNING SCHEME

A. OVERVIEW OF THE PROPOSED SCHEME

The proposed scheme compensates for the residual reactance in the receiver without communication. The comparison between the conventional receiver-side resonant frequency tuning scheme using a FET bridge-based variable reactor and the proposed scheme is shown in Fig. 1.

A capacitor C_A is connected to a half-bridge in conventional receiver-side resonant frequency tuning schemes as shown in Fig. 1(a). The gate-drive signal for the half-bridge has a duty cycle of 50% and the phase is 0° or 180° relative to the transmitter voltage source. The DC voltage of the capacitor V_{cap} is automatically adjusted to be orthogonal to the receiver current I_{RX}, which is necessary to compensate for the reactance in the receiver circuit [20]. The reference for the gate-drive signal phase is the transmitter voltage source. Therefore, the transmitter voltage-source phase must be transmitted to the receiver.

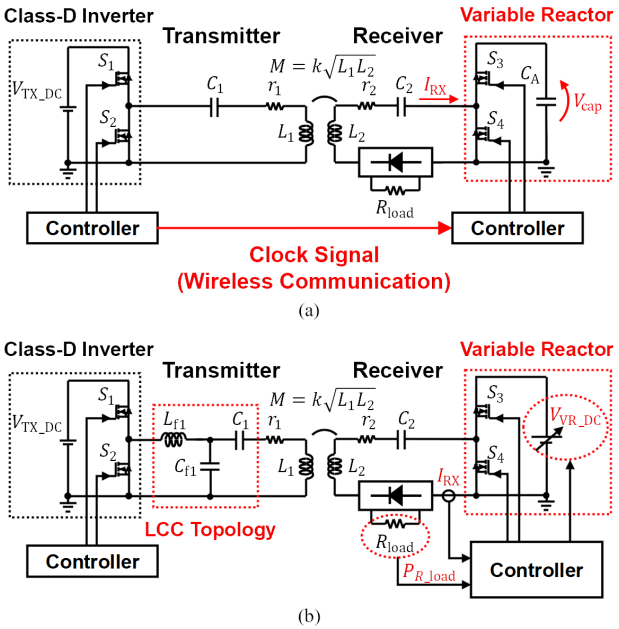

FIGURE 1. FET bridge-based variable reactor in the receiver. (a) Conventional scheme. (b) Proposed scheme.

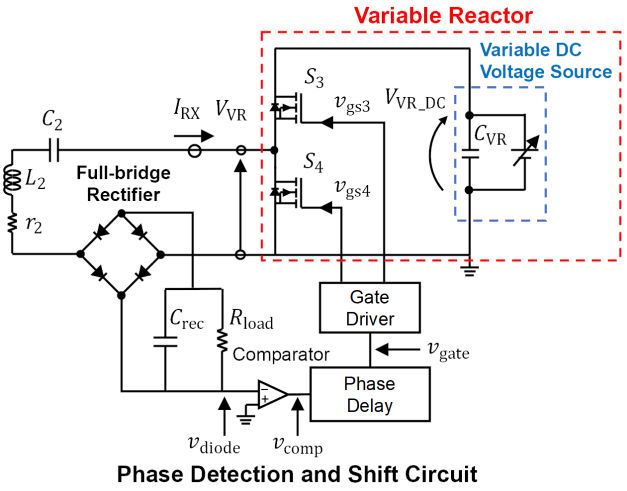

FIGURE 2. Schematic of a receiver with a FET bridge-based variable reactor.

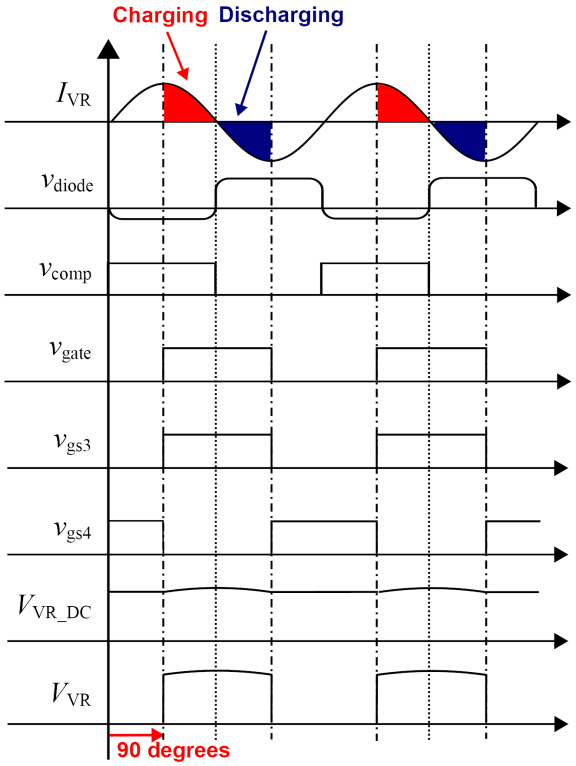

FIGURE 3. Operating waveforms of a FET bridge-based variable reactor.

Conversely, the phase reference is the receiver current in the proposed scheme as shown in Fig. 1(b). The gate-drive signal for the half-bridge circuit is generated at the receiver using the phase of the receiver current. The phase of the gate-drive signal is shifted from the phase of the receiver current by 90° or −90° depending on the sign of the resonant frequency deviation. A variable DC voltage source $V_{\mathrm{VR\_DC}}$ is connected to the half-bridge instead of the capacitor. The reactance can be adjusted by changing the DC voltage applied to the half-bridge because the output voltage of the variable reactor and the receiver current are orthogonal.

The DC voltage $V_{\mathrm{VR\_DC}}$ should be controlled to generate an appropriate reactance to cancel the residual reactance in the receiver without communication. Therefore, an LCC compensation topology is adopted in the transmitter to operate the receiver circuit with CV characteristics. The change in reactance in the circuit appears as a change in the received power at the load when the receiver circuit is driven by the CV characteristics. The received power at load resistance R_{load} is maximized when the resonant condition is achieved. Therefore, we can detect the optimal $V_{\mathrm{VR\_DC}}$ using the received power P_{R_load} as the objective function. This structure achieves resonant-frequency tuning on the receiver side without communication.

B. FET BRIDGE-BASED VARIABLE REACTOR CONTROLLED BY A DC-VOLTAGE SOURCE

The circuit structure of the receiver with the FET bridge-based variable reactor is shown in Fig. 2. The current phase-detection and phase-shift circuits are applied to detect the phase of I_{RX} and generate the gate-drive signal for the half-bridge. The operating waveforms of the current-phase-detection and phase-shift circuits are shown in Fig. 3. The phase of I_{RX} is obtained from the voltage v_{diode}, which is generated when I_{RX} conducts through one of the diodes of the rectifier circuit. The comparator detects zero crossings of I_{RX} using v_{diode} and generates the input signal for the phase shift circuit, v_{comp}. Subsequently, the phase-shift circuit generates the input signal to the half-bridge circuit v_{gate} by delaying the output of the comparator. The amount of phase

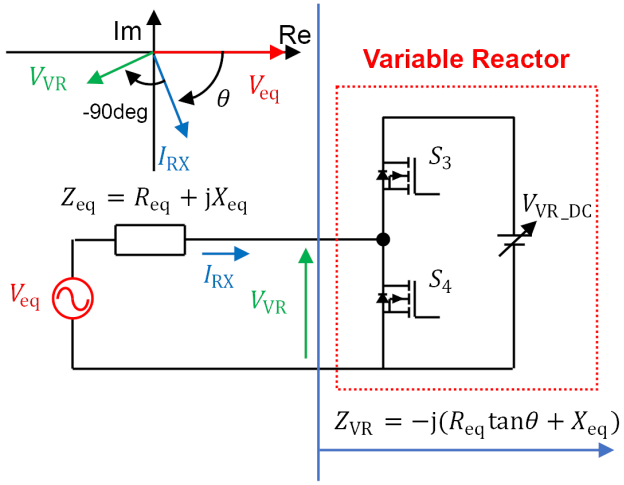

FIGURE 4. Variable reactor with the connected equivalent voltage and impedance.

shift depends on whether the reactance to be compensated for is inductive or capacitive. To compensate for inductive reactance, the phase shift is set to 90°, whereas, to compensate for capacitive reactance, it is set to −90° (270°). Fig. 3 shows the operating waveforms indicating that the variable reactor behaves similarly to a capacitor to compensate for the inductive reactance.

The variable DC voltage source is implemented along with an output capacitor C_{VR}. The driving power of the variable DC voltage source is provided by an internal power supply equipped with a receiver, such as a battery. Notably, the variable DC voltage source does not provide active power in the steady state. Consequently, the power supply of the receiver to drive the variable DC voltage source does not consume any power except for the power consumption of related circuits such as a gate driver and microprocessor. This consumption is constant regardless of the output power of the wireless power transfer system. Once the output capacitor C_{VR} is charged to a designated voltage, no power flows from the power supply of the receiver. In other words, only the charging and discharging of C_{VR} by I_{RX} is repeated. As the phase of the switching is orthogonal to the current flows into the variable reactor, the amount of electric charge that flows into and out of C_{VR} is constant.

Herein, we derive the relationship between the impedance of the variable reactor and the DC voltage applied to the half-bridge. We adopt the first harmonic analysis in the derivation, expressed below. We assume that V_{eq} and $Z_{eq} = R_{eq}+jX_{eq}$ are connected to the variable reactor, as shown in the equivalent circuit in Fig. 4. V_{eq} and Z_{eq} are the equivalent input voltage and impedance of the receiver, respectively. $Z_{VR} = R_{VR} + jX_{VR}$ is the impedance of the variable reactor. The receiver current I_{RX} is expressed as:

$$I_{RX} = I_{RX\_m}e^{j\theta}, \tag{1}$$

where I_{RX_m} is the amplitude of I_{RX} and θ is the phase difference between V_{eq} and I_{RX}. The domain of θ is $-\pi/2 \le \theta \le \pi/2$. We fixed the phase of the output voltage of the variable reactor V_{VR} shifted by $-\mathrm{sgn}(X_{eq})\pi/2$ from I_{RX}. Therefore, V_{VR} can be calculated as follows:

$$V_{VR} = \frac{2}{\pi}V_{VR\_DC}e^{j(\theta-\mathrm{sgn}(X_{eq})\frac{\pi}{2})}. \tag{2}$$

From (1) and (2), I_{RX_m} and θ can be calculated by applying Kirchhoff's voltage law in the equivalent circuit shown in Fig. 4. The circuit equation is

$$V_{eq} = (R_{eq} + jX_{eq})I_{RX} + V_{VR}. \tag{3}$$

Substituting (1) and (2) into (3), we obtain

$$V_{eq} = (R_{eq} + jX_{eq})I_{RX\_m}e^{j\theta} + \frac{2}{\pi}V_{VR\_DC}e^{j(\theta-\mathrm{sgn}(X_{eq})\frac{\pi}{2})}. \tag{4}$$

We express (4) using trigonometric functions:

$$V_{eq} = (R_{eq} + jX_{eq})I_{RX\_m}\{\cos\theta + j\sin\theta\} - \frac{2}{\pi}V_{VR\_DC}\{\cos\theta + j\sin\theta\}\mathrm{sgn}(X_{eq})j. \tag{5}$$

Separating the real and imaginary components of (5) results in

$$V_{eq} = I_{RX\_m}(R_{eq}\cos\theta - X_{eq}\sin\theta) + \mathrm{sgn}(X_{eq}) \times \frac{2}{\pi}V_{VR\_DC}\sin\theta, \tag{6}$$

$$0 = I_{RX\_m}(X_{eq}\cos\theta + R_{eq}\sin\theta) - \mathrm{sgn}(X_{eq}) \times \frac{2}{\pi}V_{VR\_DC}\cos\theta. \tag{7}$$

From (7), I_{RX_m} can be calculated as follows:

$$I_{RX\_m} = \mathrm{sgn}(X_{eq})\frac{2}{\pi}V_{VR\_DC}\frac{1}{R_{eq}\tan\theta + X_{eq}}. \tag{8}$$

Substituting (8) into (6), we obtain

$$V_{VR\_DC} = \mathrm{sgn}(X_{eq})\frac{\pi V_{eq}}{2R_{eq}}(R_{eq}\sin\theta + X_{eq}\cos\theta). \tag{9}$$

From (1), (2), (4), and (9), the impedance of the variable reactor is calculated as follows:

$$Z_{VR} = \frac{V_{VR}}{I_{RX}} = -j(R_{eq}\tan\theta + X_{eq}). \tag{10}$$

(9) can be rewritten as

$$\theta = \arcsin\left(\mathrm{sgn}(X_{eq})\frac{2R_{eq}V_{VR\_DC}}{\pi\sqrt{R_{eq}^2 + X_{eq}^2}V_{eq}}\right) - \arctan\left(\frac{X_{eq}}{R_{eq}}\right). \tag{11}$$

(11) implies that θ and Z_{VR} can be adjusted by changing V_{VR_DC}. V_{VR_DC} must be controlled to produce the optimal reactance that compensates for X_{eq}. Based on (10), Z_{VR} becomes $-jX_{eq}$ when $\theta = 0$. Suppose V_{eq}, R_{eq}, and X_{eq} are provided. In that case, we can determine the optimal V_{VR_DC} from (9) by substituting $\theta = 0$. However, R_{eq} and X_{eq} cannot be measured in practice. Therefore, we focus on the fact that the received power at the load is maximized when X_{eq} is compensated for.

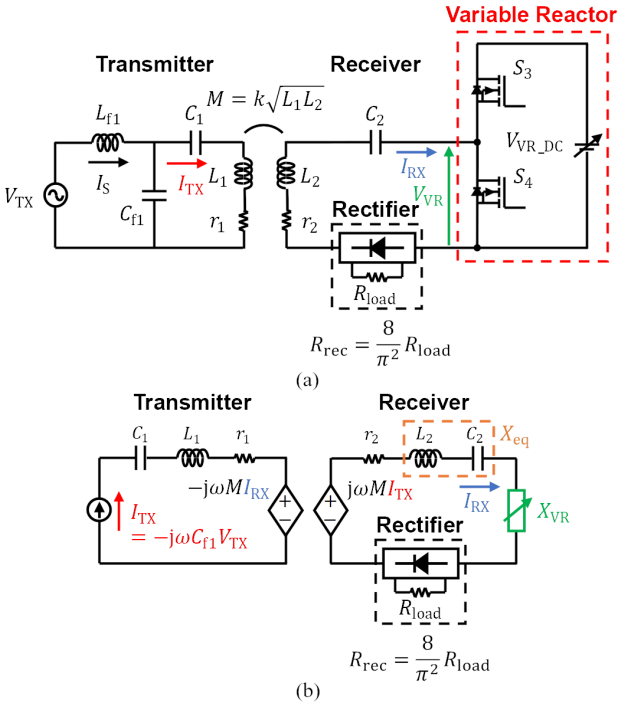

FIGURE 5. Equivalent circuit of the proposed scheme. (a) Schematic based on coupling. (b) Schematic based on induced voltage.

C. LCC COMPENSATION TOPOLOGY AT THE TRANSMITTER

Four representative compensation topologies exist, series-series (SS), series-parallel (SP), parallel-series (PS), and parallel-parallel (PP) [31]. The SS compensation topology is most widely used for MRC-WPT owing to its simplicity and low cost. Unfortunately, the SS compensation topology is not applicable to the proposed scheme because it provides CC output characteristics at the receiver. Under the CC characteristics of the receiver, the variation in the power received by the load cannot be observed even when the residual reactance is compensated for. Furthermore, SP, PS, and PP topologies cannot be used as well because they do not provide the CV output characteristic at the receiver.

We applied the LCC compensation topology at the transmitter to obtain the CV characteristics of the receiver. The LCC compensation topology provides a constant current (CC) for the transmitter coil [32], [33]; thus, a CV is induced on the receiver coil. The CV output characteristic at the receiver enables the detection of the optimal V_{VR_DC} by observing the received power at the load because the reactance fluctuation at the receiver influences the received power. Notably, detuning of the transmitter coil in the transmitter-side LCC compensation topology can be ignored because the output impedance of the CC source is extremely high. Thus, the proposed scheme functions as appropriate regardless of the residual reactance generated by the inductance change at the transmitter coil.

The equivalent circuit of the WPT system with the proposed scheme is shown in Fig. 5. The LCC compensation topology shown in Fig. 5(a) can supply a CC to the transmitter coil as shown in Fig. 5(b), regardless of the receiver conditions and transmitter coil detuning. When $\omega L_{f1} - 1/\omega C_{f1} = 0$ is valid, the transmitter coil current I_{TX} is expressed as [32]

$$I_{TX} = -j\omega C_{f1} V_{TX}, \tag{12}$$

regardless of the detuning of L_1. Consequently, the induced voltage on the receiver is expressed as

$$V_{eq} = j\omega M I_{TX} = \omega^2 M C_{f1} V_{TX}. \tag{13}$$

The equivalent impedance Z_{eq}, connected to the variable reactor is the same as the impedance in the receiver circuit:

$$Z_{eq} = R_{eq} + jX_{eq} = r_2 + R_{rec} + j\left(\omega L_2 - \frac{1}{\omega C_2}\right), \tag{14}$$

where

$$R_{rec} = \frac{8}{\pi^2} R_{load}. \tag{15}$$

The equivalent resistance R_{eq} includes the parasitic resistance of the receiver coil r_2 and the resistance of the rectifier R_{rec}. In this analysis, the rectifier is modeled as an ideal full-bridge rectifier with four Schottky barrier diodes [34]. The equivalent reactance X_{eq} includes the receiver coil L_2 and compensation capacitors C_2. A full-bridge rectifier can be precisely analyzed without considering the parasitic capacitance of Schottky barrier diodes [34], [35].

D. COMMUNICATION-LESS DC VOLTAGE CONTROL ALGORITHM

Herein, we clarify the effect of the residual reactance in the receiver on the received power and power transfer efficiency. The received power P_{R_load} and the power transfer efficiency η of the LCC-S topology are derived as [10]:

$$P_{R\_load} = \frac{M^2 {V_{TX}}^2 R_{rec}}{{L_{f1}}^2 \left({r_2}^2 + 2r_2 R_{rec} + (X_{eq} + X_{VR})^2 + {R_{rec}}^2\right)}, \tag{16}$$

$$\eta = \frac{M^2 \omega^2 R_{rec}}{M^2 \omega^2 (r_2 + R_{rec}) + r_1 (r_2 + R_{rec})^2 + r_1 (X_{eq} + X_{VR})^2}. \tag{17}$$

According to (16) and (17), the received power and power transfer efficiency are maximized when $X_{eq} + X_{VR}$ equals zero. Notably, (16) and (17) are independent of the reactance on the transmitter side; thus, the detuning of the transmitter coil is not related to the efficiency. Notably, the efficiency η is defined using the transmitter power after the DC-AC power conversion; the switching and conduction losses at the primary inverter are not considered. Suppose the switching and conduction losses are considered. In that case, the detuning of the transmitter coil influences the efficiency. Although the detuning of the transmitter coil is not addressed, a zero voltage switching class-D amplifier operating over a wide impedance range [36] or a self-tuning technique for the transmitter-side LCC topology [17] can be used as a remedy.

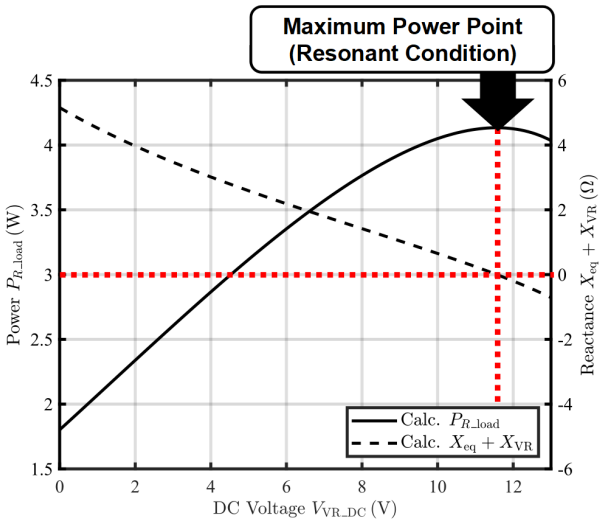

FIGURE 6. Example of the received power at the load and the residual reactance with respect to the DC voltage applied to the half-bridge.

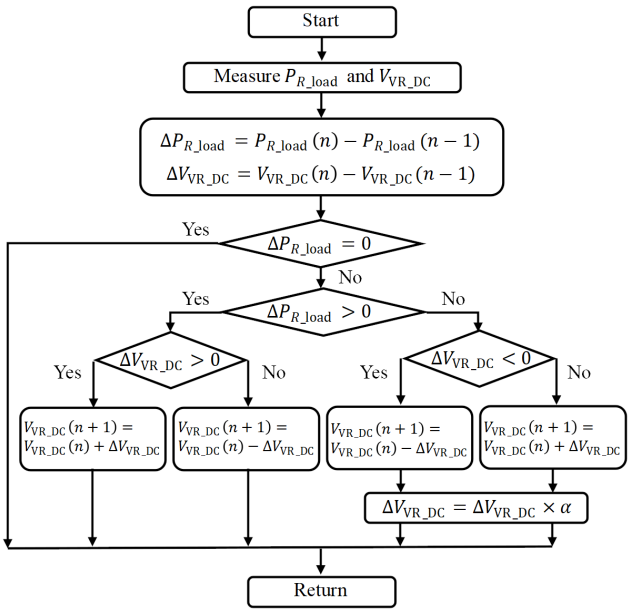

FIGURE 7. Flowchart of DC voltage control.

We used the received power P_{R_load} as the objective function to control the DC voltage V_{VR_DC} applied to the variable reactor. The received power P_{R_load} can also be written as a function with respect to V_{VR_DC} using (8) and (11):

$$P_{R\_load}(V_{VR\_DC}) = \left(\frac{I_{RX\_m}}{\sqrt{2}}\right)^2 R_{rec} = \frac{V_{eq}^2 R_{rec}}{2R_{eq}^2}\cos^2\theta(V_{VR\_DC}). \quad (18)$$

An example of the relationships between V_{VR_DC} and the residual reactance in the receiver $X_{eq} + X_{VR}$ with respect to P_{R_load} is shown in Fig. 6, which are calculated using (10), (11), and (18). In this example, the secondary series compensation capacitance in the receiver C_2 is deliberately deviated by approximately +20% from the resonant condition. $X_{eq} + X_{VR}$ becomes zero when P_{R_load} is maximized. The optimal DC voltage for reactance compensation can be detected by sweeping V_{VR_DC} to maximize P_{R_load} because P_{R_load} is convex upward and maximized when $\theta = 0$ and $Z_{VR} = -jX_{eq}$. P_{R_load} can be measured at the receiver load. Therefore, no feedback information is required from the transmitter. Notably, the efficiency (17) is also maximized when $Z_{VR} = -jX_{eq}$ and P_{R_load} are maximized.

We adopted maximum power point tracking (MPPT) control using the hill climbing method to adjust the DC voltage applied to the half-bridge. The flowchart of DC voltage control is shown in Fig. 7. The received power at load P_{R_load} is measured repeatedly using the load's output voltage. V_{VR_DC} is determined based on the sign of ΔP_{R_load}, which is the difference in P_{R_load} before and after changing V_{VR_DC}.

Initially, V_{VR_DC} gradually increased from 0 V. The direction of perturbation is maintained for the subsequent step provided the received power increases; otherwise, the direction is reversed and the change step of the DC voltage ΔV_{VR_DC} is multiplied by coefficient α, whose value is less than unity. This process is repeated until V_{VR_DC} reaches the maximum power point.

III. MEASUREMENTS AND SIMULATIONS

A. EXPERIMENTAL SETUP

We implemented a WPT system, assuming the operating frequency of a mobile charger at 200 kHz to experimentally demonstrate the functionality of the proposed scheme. Photographs of the experimental setup are shown in Fig. 8 and its schematic is shown in Fig. 9. The parameters of the components used in the measurement are listed in Table 1. The secondary series-compensation capacitance C_2 intentionally deviated from −20% to +20% from the resonant condition to validate the reactance compensation ability of the proposed scheme. Practically, the capacitance and inductance of the coils may deviate. However, we only deviate the capacitance in the experiments to ease measurements. A circuit simulation model was implemented in LTspice, using the same parameters as in the measurement.

The top views of the transmitter and receiver are shown in Fig. 8(b). The transmitter comprises a Class-D half-bridge power converter (EPC9203, EPC), DE0-Nano FPGA (Terasic) to generate the gate-drive signal, LCC compensation circuit, and transmitter coil. The EPC9203 board includes an input capacitor of 3 μF (C_{TX} and C_{VR} in Fig. 9). Polypropylene film capacitors (R75 or R76 series, KEMET) were used in the LCC compensation circuit. A leaded inductor (ELC18B5R6L, Panasonic) was used as the inductor. The receiver comprised a receiver coil, a full-bridge rectifier with a comparator (LT1711, Analog Devices) to extract the phase of the receiver current, DE0 FPGA (Terasic) for phase shift, and a variable reactor (EPC9203). The full-bridge rectifier

TABLE 1. Circuit parameters.

Parameter	Value	Description
f	200 kHz	Operating frequency
k	0.118	Coupling coefficient
$V_{\mathrm{TX\_DC}}$	24 V	Primary DC-input voltage
L_1	24.40 μH	Primary coil inductance
C_1	34.66 nF	Primary series-compensation capacitance
r_1	0.16 Ω	Primary parasitic resistance
L_{f1}	6.27 μH	Primary compensation inductance
C_{f1}	102.27 nF	Primary parallel compensation capacitance
L_2	24.44 μH	Secondary coil inductance
C_2	Variable	Secondary series-compensation capacitance
r_2	0.20 Ω	Secondary parasitic resistance
R_{load}	5 Ω	Load resistance
$V_{\mathrm{VR\_DC}}$	Variable	DC voltage applied to a variable reactor

was implemented using diodes (PMEG2020EH, Nexperia) and a 47 μF ceramic capacitor. An electronic load (LN-300A, KEISOKU GIKEN) was used as the load. Qi standard compliant coils (WT505090-20K2-A10-G, TDK) were used as Tx and Rx coils.

The front view of the experimental setup is shown in Fig. 8(a). We used a DC-voltage source (PSW-1080M160, TEXIO) as the input power source and a source-measurement unit (Model 2450, Keithley) as the receiver-side DC-voltage source for the variable reactor. The source measure unit can simultaneously adjust the output voltage and precisely measure the loss. The source measure unit is replaced by a low-power DC/DC converter or a voltage regulator in a practical system. Notably, the receiver-side DC-voltage source is not required to provide active power but only the voltage. Therefore, a bulky DC/DC converter with an inductor, which is generally used as a power source, is not required. Instead, a small and low-power DC/DC converter, such as an inductor-less charge pump DC/DC converter or a voltage regulator using an operational amplifier, which can be implemented in the form of an integrated circuit, are promising candidates.

The DC input and output power were measured using a power analyzer (PW3390, Hioki E.E. Corp.). The operating waveforms were observed using an oscilloscope (MDO4054-3, Tektronix). For automatic control, the received power was measured with the output voltage at the load using an Arduino Nano board and the measured value was transmitted to a laptop PC. When automatic control was enabled, the laptop PC sent commands to the source measure unit to change the DC voltage. In this measurement, evaluation boards were used to implement the related circuits for phase delay and reactance control because of the ease of prototyping. They can be implemented on one board in a practical system, downsizing the entire system volume.

B. DEFINITION OF POWER TRANSFER EFFICIENCY

First, we define the power transfer efficiency considering the loss at the variable reactor. Ideally, the variable reactor does not consume active power because the phase of the output voltage is orthogonal to the input current. In particular, the amount of current that flows into and from the DC voltage source is the same. However, the actual variable reactor

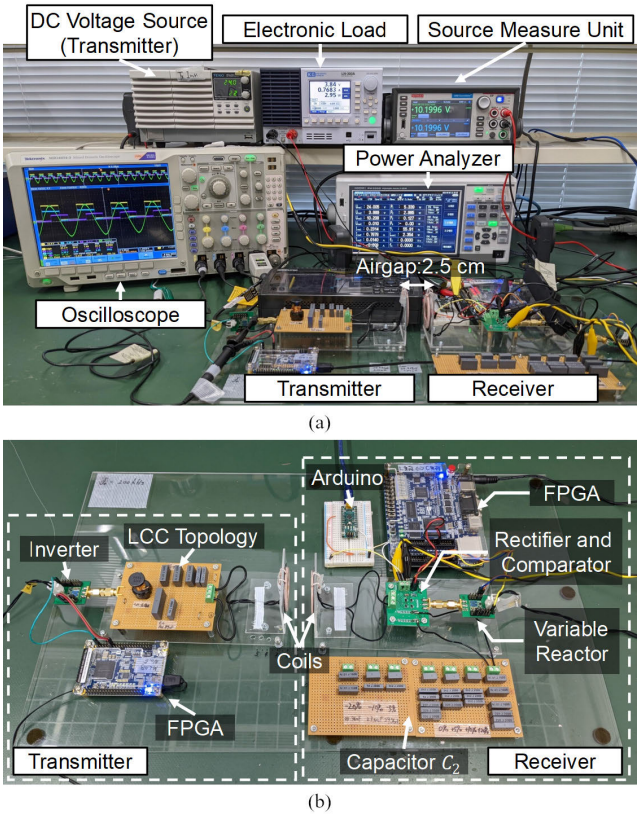

FIGURE 8. Experimental setup. (a) Front view. (b) Top view.

slightly consumes active power owing to the phase shift error. The power transfer efficiency considering the loss at the variable reactor is defined as follows:

$$\eta_{sys} = \begin{cases} (P_{R\_\mathrm{load}} - |P_{\mathrm{VR}}|)/P_{\mathrm{TX}}, & P_{\mathrm{VR}} < 0, \\ P_{R\_\mathrm{load}}/P_{\mathrm{TX}}, & P_{\mathrm{VR}} \geq 0, \end{cases} \tag{19}$$

where P_{TX} denotes the input power from the transmission power supply and P_{VR} denotes the power consumed or provided by the variable reactor. The positive P_{VR} indicates that the active power is consumed at the variable reactor, the same as other losses in the receiver. Notably, P_{VR} can be negative. When P_{VR} is negative, active power flows from the variable DC voltage source. In this case, we subtract the absolute value of P_{VR} from P_{R_load} in the numerator of (19) because we assume that P_{VR} is provided from the received power P_{R_load}.

The power consumption of related circuits, such as a gate driver and microprocessor, is not considered in this definition. This might influence the total system efficiency when the transmitted power is quite small. However, the power consumption of related circuits can be neglected when the transmitted power is relatively high because it is constant regardless of the transmitted power.

C. RECEIVED POWER CHARACTERISTICS AND OPERATING WAVEFORM

Here, we evaluated the received power P_{R_load} at the load and reactance $X_{\mathrm{eq}} + X_{\mathrm{VR}}$ in the receiver with respect to the

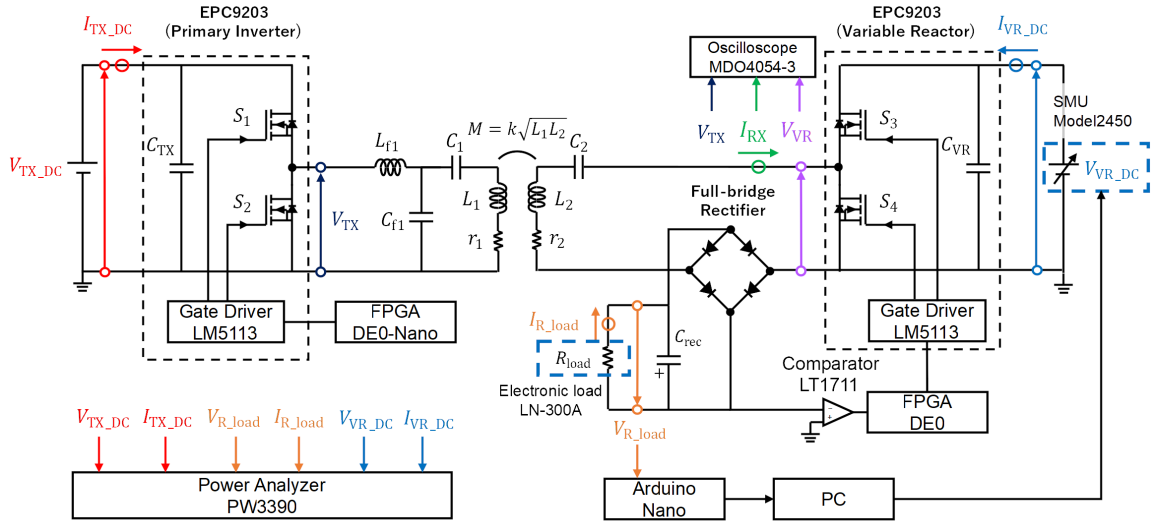

FIGURE 9. Schematic of the experimental setup.

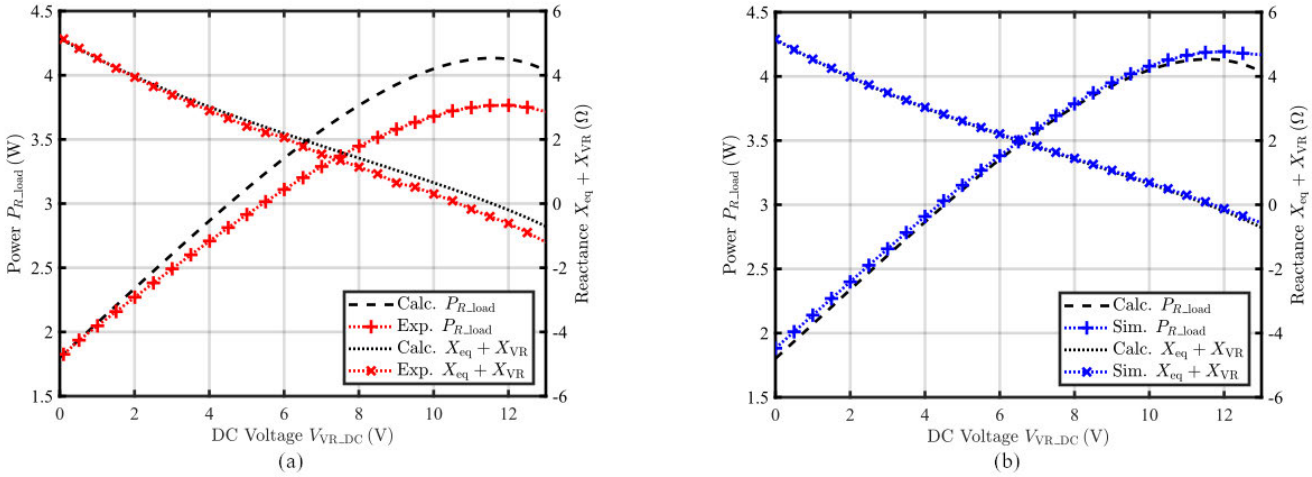

FIGURE 10. Received power at the load and the reactance in the receiver. (a) Measured. (b) Simulated.

DC voltage variation at the variable reactor. The secondary capacitor was set to 31.12 nF (+20%).

The measured and simulated received power P_{R_load} and reactance $X_{eq} + X_{VR}$ are shown in Figs. 10(a) and 10(b), respectively. The DC voltage V_{VR_DC} applied to the half-bridge is increased from 0 V to 13.0 V. The impedance of the variable reactor was calculated using V_{VR} and I_{RX} measured using the oscilloscope. The measured and simulated received power exhibit similar peak characteristics when $X_{eq}+X_{VR}$ approached 0 Ω. As V_{VR_DC} increased, $X_{eq}+X_{VR}$ decreased toward the capacitive region. In the measurement results, the received power P_{R_load} increased gradually as V_{VR_DC} increased until V_{VR_DC} reached 12.0 V. At the maximum power point of the measured result, $P_{R\_load} = 3.60$ W. The measured impedance of the variable reactor $R_{VR} + jX_{VR}$ is $0.18 - j5.77\,\Omega$ at $V_{VR\_DC} = 12.0$ V. In the simulation results, the maximum received power is 4.20 W when $V_{VR\_DC} = 12.0\,V$. The simulated impedance of the variable reactor is $-0.02 - j5.26\,\Omega$ when $V_{VR\_DC} = 12.0$ V.

Without compensation, the reactance in the receiver is $X_{eq} = \omega L_2 - 1/(\omega C_2) = 5.17\,\Omega$. Hence, the total reactance $X_{eq} + X_{VR}$ in the receiver is calculated as $-0.60\,\Omega$ for the measurement and $-0.09\,\Omega$ for the simulation. Different from the simulated result, the peak power of the experiment is lower than that of the simulation by approximately 0.60 W. This does not result from the loss in the variable reactor but from the measurement error of the coupling coefficient. Notably, the measurement error of the coupling coefficient does not influence the functionality of the proposed scheme.

Table 2 compares the power transfer efficiency among three conditions:

ID1) Without a variable reactor, $C_2 = 31.12$ nF (+20% error)

ID2) Without a variable reactor, $C_2 = 25.88$ nF (resonance)

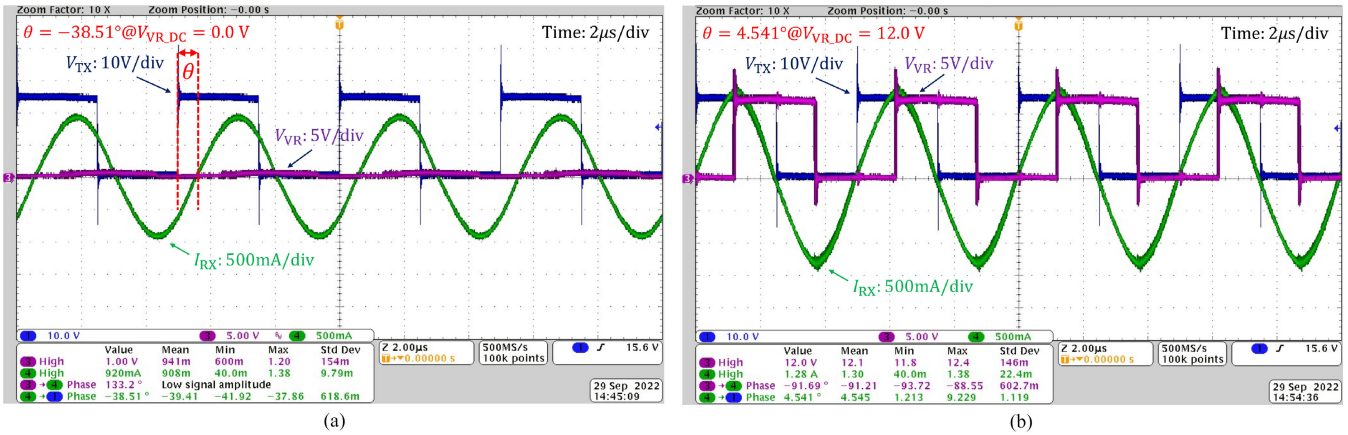

(a) (b)

FIGURE 11. Experimental waveforms. (a) Without compensation. (b) Compensated with the variable reactor.

TABLE 2. Comparison of the power transfer efficiency.

ID	C_2	X_{eq}	Measurement				Simulation			
			X_{VR}	P_{R_load}	P_{VR}	η_{sys}	X_{VR}	P_{R_load}	P_{VR}	η_{sys}
1 (Without compensation)	31.12 nF	5.17 Ω	-	1.78 W	-	52.7 %	-	1.83 W	-	57.6 %
2 (Resonance)	25.88 nF	−0.04Ω	-	3.73 W	-	62.7 %	-	4.17 W	-	68.4 %
3 (Compensated with VR)	31.12 nF	5.17 Ω	−5.77 Ω	3.60 W	−0.03 W	60.3 %	−5.26 Ω	4.20 W	−0.10 W	68.5 %

ID3) With a variable reactor, $C_2 = 31.12$ nF (+20% error); $V_{\mathrm{VR\_DC}}$ is set to 12.0 V, which is the maximum power point.

In the case without a variable reactor (ID1), the received power and power transfer efficiency are 1.78 W and 52.7% as per the measurement results, and 1.83 W and 57.6% as per the simulation results, respectively. Comparing ID1 (without a variable reactor) and ID3 (compensated with a variable reactor), the efficiency was improved by 14.4% in the measurement and 18.9% in the simulation. In the measurement, although the efficiency of ID3 was slightly degraded from that of ID2 (resonance), the power transfer efficiency can be improved from ID1 by applying the proposed scheme and compensating for the reactance in the receiver.

The operating waveforms of V_{TX}, V_{VR} and I_{RX} at $V_{\mathrm{VR\_DC}} = 0$ V and $V_{\mathrm{VR\_DC}} = 12.0$ V are shown in Figs. 11(a) and 11(b). At $V_{\mathrm{VR\_DC}} = 0$ V, the phase difference θ between the input voltage V_{TX} and receiver current I_{RX} is $-38.51°$ in Fig. 11(a). However, θ becomes 4.54° at $V_{\mathrm{VR\_DC}} = 12.0$ V, as shown in Fig. 11(b). Evidently, the amplitude of I_{RX} increased as the phase difference θ decreased. The phase difference between V_{VR} and I_{RX} is 91.21°, as shown in Fig. 11(b). We validated that V_{VR} is orthogonal to I_{RX} regardless of $V_{\mathrm{VR\_DC}}$, by sweeping $V_{\mathrm{VR\_DC}}$ from 0 V to 13 V.

Therefore, the residual reactance in the receiver was suppressed and we could determine $V_{\mathrm{VR\_DC}}$ for reactance compensation using the peak of the received power at the load. Theoretically, $X_{\mathrm{eq}} + X_{\mathrm{VR}}$ should be zero when the received power is maximum. The difference between the measured results and the theoretical calculation can be attributed to errors in the phase shift by the comparator and the fabrication of the LCC compensation topology at the transmitter.

D. AUTOMATIC DC VOLTAGE CONTROL

The functionality of the automatic DC-voltage control using the hill climbing algorithm was evaluated, assuming the positions of the coil remained unchanged. The change in the DC voltage and the received power at the load is shown in Fig. 12. The initial change step of the DC voltage $\Delta V_{\mathrm{VR\_DC}}$ was set to 0.8 V and the coefficient α was set to 0.85. DC voltage control started at $t = 1$ s. Further, the DC voltage increased every 0.25 s. Notably, the update interval was constrained by the communication delay and response time of the source measure unit used as the DC-voltage source, which can be shortened in practical implementation. The output voltage of the load increased with an increase in the DC voltage of the variable reactor. At $t = 15$ s, the DC voltage of the variable reactor converged to 11.2 V. The output voltage of the load converged to 4.62 V. The received power at the load is calculated as 4.27 W. Using the static measurement from III-C, the maximum power point obtained was $V_{\mathrm{VR\_DC}} = 12.0$ V, which is almost the same as that for automatic DC-voltage control. Consequently, the effectiveness of the automatic DC-voltage-control algorithm was validated.

Suppose the positions change. In that case, the coupling between the coils also changes, resulting in a change in the received power. When the positions change instantaneously, the hill climbing algorithm might fail to track the maximum power point. Therefore, the control must recommence if an instantaneous change in the received power is detected. The change in the received power resulting from the DC voltage

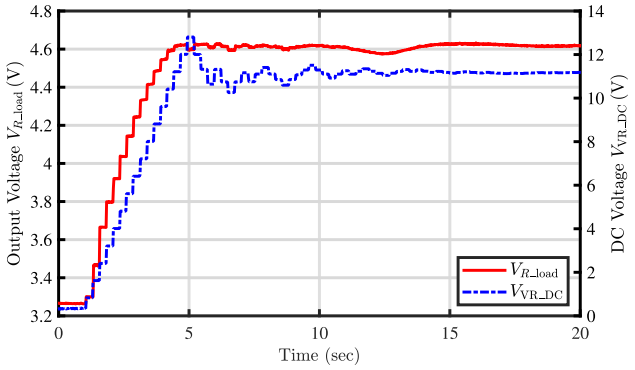

FIGURE 12. Results of automatic DC voltage control.

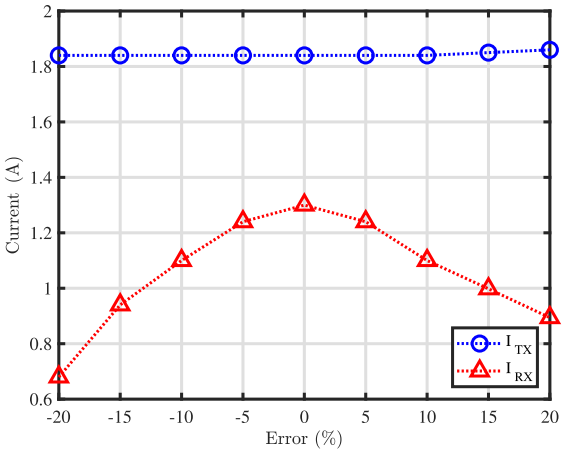

FIGURE 13. Measured transmitter and receiver current variation without the variable reactor against secondary capacitance errors.

control is relatively small and can be predicted. However, a sudden change in position will result in a significant change in the received power, which has significantly different characteristics from the change when the DC voltage is gradually adjusted.

E. EVALUATION OF VARIOUS CAPACITANCE ERRORS

Finally, we conducted measurements for various capacitance error conditions. The secondary capacitance deviated from the resonant condition (25.88 nF) by −20% (20.19 nF) to +20% (31.12 nF).

We evaluated the constant current characteristics of the LCC compensation topology before the measurements with the variable reactor. The transmitter current I_{TX} and the receiver current I_{RX} for various capacitance errors were measured without the variable reactor. The variation of I_{TX} and I_{RX} is shown in Fig. 13. I_{RX} decreased with detuning, whereas I_{TX} remained unchanged. These results validate the CC characteristics at the transmitter side owing to the LCC compensation topology.

Next, we investigated the effectiveness of reactance compensation by the variable reactor compared with the passive compensation without the variable reactor. The received

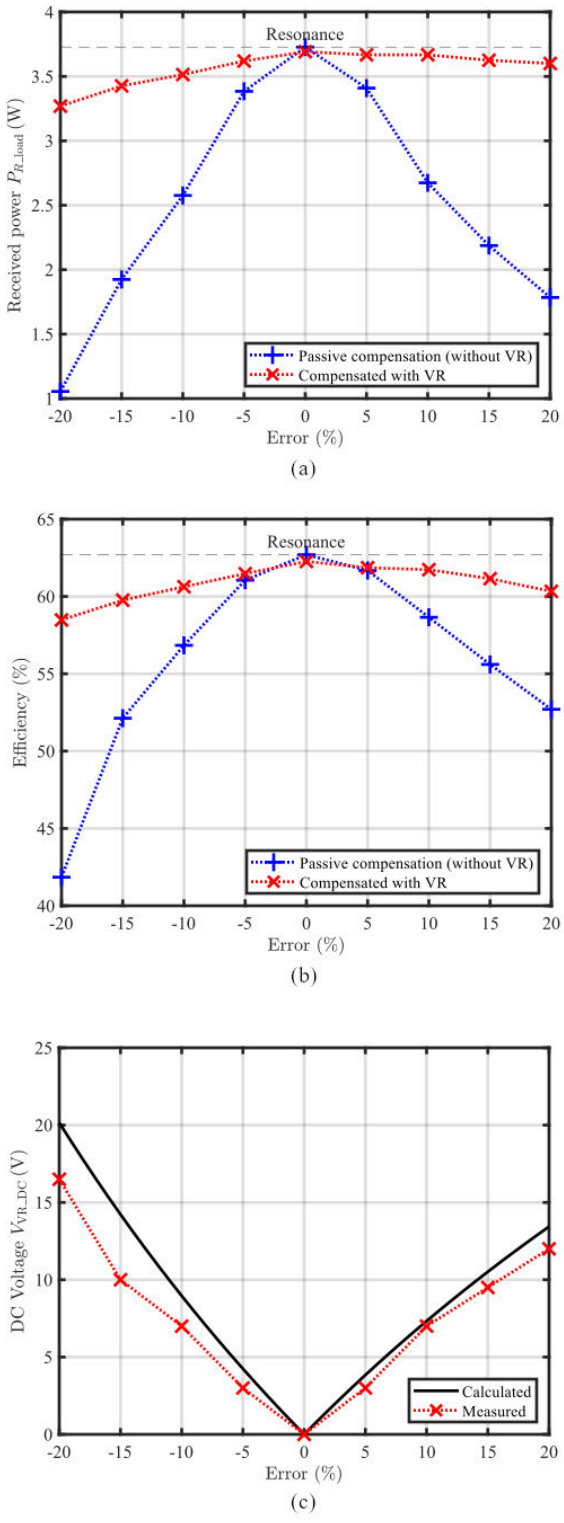

FIGURE 14. Measurement results for various capacitance deviations. (a) Received power. (b) Power transfer efficiency. (c) DC voltage required for reactance compensation.

power against capacitance errors is shown in Fig. 14(a). The power transfer efficiency against capacitance errors is shown in Fig. 14(b). The DC voltage of the variable reactor was

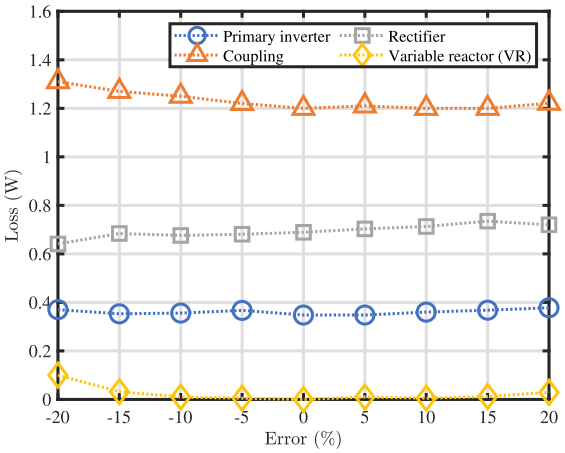

FIGURE 15. Measured loss distribution against capacitance errors.

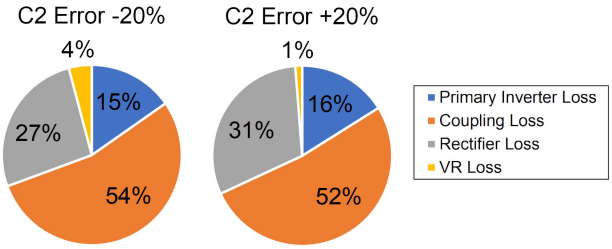

FIGURE 16. Loss breakdown for the −20% and +20% errors.

determined to maximize the received power in each capacitance error condition, which is shown in Fig. 14(c). The theoretical value of the DC voltage was calculated using (9).

The power and efficiency of the proposed scheme are maintained nearly constant regardless of secondary capacitance detuning, whereas that of the passive compensation without the variable reactor significantly decreased with the capacitance error. Even after compensation with the variable reactor, the power and efficiency slightly degrade as the detuning increases because of the loss at the variable reactor. However, the degradation of power and efficiency is apparently mitigated compared with passive compensation; for example, even when the efficiency without the variable reactor degraded from 62.7% to 41.8% at −20% error, the efficiency with the variable reactor was maintained to 58.5%. When the secondary capacitance deviated from −20% to +20%, the degradation of efficiency from the resonant condition was maintained within 6.7% by applying the variable reactor, whereas the efficiency degraded by up to 33.3% without the variable reactor.

The loss distribution of the experimental prototype against capacitance errors is shown in Fig. 15, whereas the loss breakdown for the −20% and +20% errors is shown in Fig. 16. In both cases, the loss of the variable reactor is considerably small compared with the primary inverter, coupling, and rectifier losses. Comparing the positive (>0%) and negative (<0%) capacitance error, the loss at the variable reactor is more significant for the negative capacitance error. When the capacitance error is negative, the equivalent reactance in the receiver X_{eq} is capacitive. Consequently, the variable reactor behaves inductive to cancel the error. However, the inductive behavior of a FET bridge-based variable reactor results in hard switching, which increases the switching loss [20]. To avoid hard switching, a higher value C_2 is required such that the variable reactor always behaves capacitive and achieves soft switching, as discussed in [25].

IV. CONCLUSION

This study proposed a communication-less resonant frequency-tuning scheme at the receiver side for a magnetically coupled WPT system. The proposed scheme compensated for the reactance in the receiver with no communication link between the transmitter and receiver. The only control parameter required was the DC received power at the load, which can be easily measured.

A class-D inverter was used as a variable reactor in the receiver by shifting the switching phase of the half-bridge by 90° from the receiver current. The LCC compensation topology was adopted on the transmitter side to obtain the CV characteristics of the receiver, which enabled communication-less control. The variable reactor was adjusted through the DC voltage applied to the half-bridge, which adopted the received power at the load as the objective function to compensate for the reactance in the receiver. Automatic DC-voltage control using a hill climbing algorithm was implemented in the experimental prototype.

The functionality of the proposed scheme was evaluated through measurements and simulations. The reactance compensation was achieved by controlling the DC voltage to maximize the received power. When the secondary capacitance deviated from −20% to +20%, efficiency degradation from the resonant condition was limited within 6.7% by applying the variable reactor, whereas the efficiency degraded by up to 33.3% without the variable reactor. The proposed scheme was evaluated under the assumption of low-power mobile device charging. However, the FET bridge-based variable reactor is expected to be suitable even for high-power applications, such as electric vehicles, because its structure is based on the class-D inverter originally used as the power source.

The proposed scheme can ensure a highly efficient power transfer under practical operating environments where various undesirable factors exist for WPT systems and improve the reliability of magnetically coupled WPT systems.

REFERENCES

[1] A. Kurs, A. Karalis, R. Moffatt, J. D. Joannopoulos, P. Fisher, and M. Soljačić, "Wireless power transfer via strongly coupled magnetic resonances," *Science*, vol. 317, no. 5834, pp. 83–86, 2007.

[2] H. Shoki, "Issues and initiatives for practical deployment of wireless power transfer technologies in Japan," *Proc. IEEE*, vol. 101, no. 6, pp. 1312–1320, Jun. 2013.

[3] S. Y. R. Hui, W. Zhong, and C. K. Lee, "A critical review of recent progress in mid-range wireless power transfer," *IEEE Trans. Power Electron.*, vol. 29, no. 9, pp. 4500–4511, Sep. 2014.

[4] Z. Zhang, H. Pang, A. Georgiadis, and C. Cecati, "Wireless power transfer-an overview," *IEEE Trans. Ind. Electron.*, vol. 66, no. 2, pp. 1044–1058, Feb. 2019.

[5] Y.-J. Kim, D. Ha, W. J. Chappell, and P. P. Irazoqui, "Selective wireless power transfer for smart power distribution in a miniature-sized multiple-receiver system," *IEEE Trans. Ind. Electron.*, vol. 63, no. 3, pp. 1853–1862, Mar. 2016.

[6] C. Liu, C. Jiang, J. Song, and K. T. Chau, "An effective sandwiched wireless power transfer system for charging implantable cardiac pacemaker," *IEEE Trans. Ind. Electron.*, vol. 66, no. 5, pp. 4108–4117, May 2019.

[7] J. Kim, H.-C. Son, D.-H. Kim, and Y.-J. Park, "Optimal design of a wireless power transfer system with multiple self-resonators for an LED TV," *IEEE Trans. Consum. Electron.*, vol. 58, no. 3, pp. 775–780, Aug. 2012.

[8] S. Li and C. C. Mi, "Wireless power transfer for electric vehicle applications," *IEEE J. Emerg. Sel. Topics Power Electron.*, vol. 3, no. 1, pp. 4–17, Mar. 2015.

[9] T. Imura, "Simple equivalent circuit model with foreign object on wireless power transfer via magnetic resonant coupling," in *Proc. IEEE Conf. Antenna Meas. Appl. (CAMA)*, Dec. 2017, pp. 367–370.

[10] R. Mai, P. Yue, Y. Liu, Y. Zhang, and Z. He, "A dynamic tuning method utilizing inductor paralleled with load for inductive power transfer," *IEEE Trans. Power Electron.*, vol. 33, no. 12, pp. 10924–10934, Dec. 2018.

[11] A. Trigui, S. Hached, F. Mounaim, A. C. Ammari, and M. Sawan, "Inductive power transfer system with self-calibrated primary resonant frequency," *IEEE Trans. Power Electron.*, vol. 30, no. 11, pp. 6078–6087, Nov. 2015.

[12] T. C. Beh, M. Kato, T. Imura, S. Oh, and Y. Hori, "Automated impedance matching system for robust wireless power transfer via magnetic resonance coupling," *IEEE Trans. Ind. Electron.*, vol. 60, no. 9, pp. 3689–3698, Sep. 2013.

[13] Y. Lim, H. Tang, S. Lim, and J. Park, "An adaptive impedance-matching network based on a novel capacitor matrix for wireless power transfer," *IEEE Trans. Power Electron.*, vol. 29, no. 8, pp. 4403–4413, Aug. 2014.

[14] J. Kim, D.-H. Kim, and Y.-J. Park, "Free-positioning wireless power transfer to multiple devices using a planar transmitting coil and switchable impedance matching networks," *IEEE Trans. Microw. Theory Techn.*, vol. 64, no. 11, pp. 3714–3722, Nov. 2016.

[15] J. Bito, S. Jeong, and M. M. Tentzeris, "A real-time electrically controlled active matching circuit utilizing genetic algorithms for wireless power transfer to biomedical implants," *IEEE Trans. Microw. Theory Techn.*, vol. 64, no. 2, pp. 365–374, Feb. 2016.

[16] H. Kennedy, R. Bodnar, T. Lee, and W. Redman-White, "A self-tuning resonant-inductive-link transmit driver using quadrature symmetric delay trimmable phase-switched fractional capacitance," *IEEE J. Solid-State Circuits*, vol. 53, no. 6, pp. 1694–1706, Jun. 2018.

[17] D.-H. Kim and D. Ahn, "Self-tuning LCC inverter using PWM-controlled switched capacitor for inductive wireless power transfer," *IEEE Trans. Ind. Electron.*, vol. 66, no. 5, pp. 3983–3992, May 2019.

[18] J. Zhang, J. Zhao, Y. Zhang, and F. Deng, "A wireless power transfer system with dual switch-controlled capacitors for efficiency optimization," *IEEE Trans. Power Electron.*, vol. 35, no. 6, pp. 6091–6101, Jun. 2020.

[19] W. Li, G. Wei, C. Cui, X. Zhang, and Q. Zhang, "A double-side self-tuning LCC/S system using a variable switched capacitor based on parameter recognition," *IEEE Trans. Ind. Electron.*, vol. 68, no. 4, pp. 3069–3078, Apr. 2021.

[20] Y. Endo and Y. Furukawa, "Proposal for a new resonance adjustment method in magnetically coupled resonance type wireless power transmission," in *IEEE MTT-S Int. Microw. Symp. Dig.*, Kyoto, Japan, May 2012, pp. 263–266.

[21] M. Ishihara, K. Umetani, and E. Hiraki, "Automatic resonance frequency tuning method for repeater in resonant inductive coupling wireless power transfer systems," in *Proc. Int. Power Electron. Conf. (IPEC-Niigata - ECCE Asia)*, May 2018, pp. 1610–1616.

[22] A. Konishi, K. Fujiki, K. Umetani, and E. Hiraki, "Resonant frequency tuning system for repeater resonator of resonant inductive coupling wireless power transfer," in *Proc. 21st Eur. Conf. Power Electron. Appl. (EPE ECCE Eur.)*, Sep. 2019, pp. 1–10.

[23] M. Ishihara, K. Fujiki, K. Umetani, and E. Hiraki, "Autonomous system concept of multiple-receiver inductive coupling wireless power transfer for output power stabilization against cross-interference among receivers and resonance frequency tolerance," *IEEE Trans. Ind. Appl.*, vol. 57, no. 4, pp. 3898–3910, Aug. 2021.

[24] L. Shi, P. Alou, J. A. Oliver, and J. A. Cobos, "A novel self-adaptive wireless power transfer system to cancel the reactance of the series resonant tank and deliver more power," in *Proc. IEEE Energy Convers. Congr. Expo. (ECCE)*, Oct. 2019, pp. 4207–4211.

[25] L. Shi, P. Alou, J. Ángel Oliver, J. Carlos Rodriguez, A. Delgado, and J. A. Cobos, "A self-adaptive wireless power transfer system to cancel the reactance," *IEEE Trans. Ind. Electron.*, vol. 68, no. 12, pp. 12141–12151, Dec. 2021.

[26] D. J. Thrimawithana, U. K. Madawala, and M. Neath, "A synchronization technique for bidirectional IPT systems," *IEEE Trans. Ind. Electron.*, vol. 60, no. 1, pp. 301–309, Jan. 2013.

[27] R. Mai, Y. Liu, Y. Li, P. Yue, G. Cao, and Z. He, "An active-rectifier-based maximum efficiency tracking method using an additional measurement coil for wireless power transfer," *IEEE Trans. Power Electron.*, vol. 33, no. 1, pp. 716–728, Jan. 2018.

[28] A. Berger, M. Agostinelli, S. Vesti, J. A. Oliver, J. A. Cobos, and M. Huemer, "A wireless charging system applying phase-shift and amplitude control to maximize efficiency and extractable power," *IEEE Trans. Power Electron.*, vol. 30, no. 11, pp. 6338–6348, Nov. 2015.

[29] C. Zhao, Z. Wang, J. Du, J. Wu, S. Zong, and X. He, "Active resonance wireless power transfer system using phase shift control strategy," in *Proc. Annu. IEEE Appl. Power Electron. Conf. Expo. (APEC)*, Mar. 2014, pp. 1336–1341.

[30] K. Matsuura, D. Kobuchi, Y. Narusue, and H. Morikawa, "Communication-less receiver-side resonant frequency tuning method for magnetically coupled wireless power transfer systems," in *Proc. IEEE Radio Wireless Symp. (RWS)*, Jan. 2021, pp. 108–111.

[31] M. A. Houran, X. Yang, and W. Chen, "Magnetically coupled resonance WPT: Review of compensation topologies, resonator structures with misalignment, and EMI diagnostics," *Electronics*, vol. 7, no. 11, p. 296, Nov. 2018.

[32] Z. Pantic, S. Bai, and S. M. Lukic, "ZCS *LCC*-compensated resonant inverter for inductive-power-transfer application," *IEEE Trans. Ind. Electron.*, vol. 58, no. 8, pp. 3500–3510, Aug. 2011.

[33] L. Jiang and D. Costinett, "A high-efficiency GaN-based single-stage 6.78 MHz transmitter for wireless power transfer applications," *IEEE Trans. Power Electron.*, vol. 34, no. 8, pp. 7677–7692, Aug. 2019.

[34] Y. Narusue, Y. Kawahara, and T. Asami, "Maximizing the efficiency of wireless power transfer with a receiver-side switching voltage regulator," *Wireless Power Transf.*, vol. 4, no. 1, pp. 42–54, Mar. 2017.

[35] M. Ito, K. Hosodani, K. Itoh, S.-i. Betsudan, S. Makino, T. Hirota, K. Noguchi, and E. Taniguchi, "High efficient bridge rectifiers in 100MHz and 2.4GHz bands," in *Proc. IEEE Wireless Power Transf. Conf.*, May 2014, pp. 64–67.

[36] M. A. de Rooij, "The ZVS voltage-mode class-D amplifier, an eGaN FET-enabled topology for highly resonant wireless energy transfer," in *Proc. IEEE Appl. Power Electron. Conf. Expo. (APEC)*, Mar. 2015, pp. 1608–1613.

KENTARO MATSUURA (Graduate Student Member, IEEE) received the B.E. and M.E. degrees in electrical engineering from The University of Tokyo, Tokyo, Japan, in 2018 and 2020, respectively. He is currently pursuing the Ph.D. degree in electrical engineering. His current research interests include magnetic resonant wireless and microwave power transfer. He is a Student Member of The Institute of Electronics, Information and Communication Engineers (IEICE). He was a recipient of the Student Best Paper Award from the Asian Wireless Power Transfer Workshop, in 2021.

DAISUKE KOBUCHI (Graduate Student Member, IEEE) received the B.E. and M.E. degrees from the Graduate School of Engineering, The University of Tokyo, Tokyo, Japan, in 2019 and 2021, respectively, where he is currently pursuing the Ph.D. degree. His research interests include wireless power transfer and chipless RFID. He is a Research Fellow of the Japan Society for the Promotion of Science, Tokyo. He is also a Student Member of The Institute of Electronics, Information and Communication Engineers (IEICE).

YOSHIAKI NARUSUE (Member, IEEE) received the B.E., M.E., and Ph.D. degrees from the Graduate School of Information Science and Technology, The University of Tokyo, Tokyo, Japan, in 2012, 2014, and 2017, respectively. He is currently a full-time Lecturer with the Department of Electrical Engineering and Information Systems, Graduate School of Engineering, The University of Tokyo. His research interests include wireless power transfer, next-generation wireless communication systems, and the Internet of Things. He is a member of The Institute of Electronics, Information and Communication Engineers (IEICE) and IPSJ. He was a recipient of the Second-Best Student Paper Award from the IEEE Radio and Wireless Symposium, in 2013, the Hiroshi Harashima Academic Encouragement Award, in 2013, the Best Paper Award at the IEEE Consumer Communications and Networking Conference, in 2018, and the ACM IMWUT Distinguished Paper Award, in 2020.

HIROYUKI MORIKAWA (Member, IEEE) received the B.E., M.E., and Dr.Eng. degrees in electrical engineering from The University of Tokyo, Tokyo, Japan, in 1987, 1989, and 1992, respectively. Since 1992, he has been with The University of Tokyo, where he is currently a Professor. He has authored or coauthored the books titled *Data-Driven Economy* and *5G*. His research interests include the Internet of Things, wireless communications, digital transformation, cloud robotics, and digital society design. He was a recipient of more than 100 honors and awards, including The Institute of Electronics, Information and Communication Engineers (IEICE) Best Paper Award (thrice), the IPSJ Outstanding Paper Award, the NTT DoCoMo Mobile Science Award, the Radio Day Ministerial Commendation, the Rinzaburo Shida Award, and the Okawa Publications Prize. He is the Chairperson of the Communications and Information Network Association of Japan, Beyond 5G New Business Strategy Center, 5G-Driven Social Design Consortium, Smart Resilience Network, Digital Society Design Council, and Information and Communication Council Working Group of the Ministry of Internal Affairs and Communications, and the President-Elect of IEICE, Tokyo. He was the Vice-Chair of the OECD Committee on Digital Economy Policy. He serves on numerous advisory committees and frequently serves as a consultant to governments and companies.